Title

Self-Assembly of a Designed Nucleoprotein Architecture through Multimodal Interactions

Journal

ACS Central Science, 4(11)

ISSN

2374-7943

Authors

Subramanian, Rohit H
Smith, Sarah J
Alberstein, Robert G
et al.

Publication Date

2018-11-28

DOI

10.1021/acscentsci.8b00745

Peer reviewed

ACS central science

Research Article

Cite This: ACS Cent. Sci. 2018, 4, 1578−1586

http://pubs.acs.org/journal/acscii

Self-Assembly of a Designed Nucleoprotein Architecture through Multimodal Interactions

Rohit H. Subramanian,[†,⊥] Sarah J. Smith,[†,⊥] Robert G. Alberstein,[†] Jake B. Bailey,[†] Ling Zhang,[†] Giovanni Cardone,[†] Lauri Suominen,[†] Mohamed Chami,[‡] Henning Stahlberg,[‡] Timothy S. Baker,[†,§] and F. Akif Tezcan*[,†,∥]

[†]Department of Chemistry and Biochemistry, University of California, San Diego, La Jolla, California 92093, United States

[‡]C−CINA, Biozentrum, University of Basel, Mattenstrasse 26, 4058 Basel, Switzerland

[§]Division of Biological Sciences, University of California, San Diego, La Jolla, California 92093, United States

[∥]Materials Science and Engineering, University of California, San Diego, La Jolla, California 92093, United States

Supporting Information

ABSTRACT: The co-self-assembly of proteins and nucleic acids (NAs) produces complex biomolecular machines (e.g., ribosomes and telomerases) that represent some of the most daunting targets for biomolecular design. Despite significant advances in protein and DNA or RNA nanotechnology, the construction of artificial nucleoprotein complexes has largely been limited to cases that rely on the NA-mediated spatial organization of protein units, rather than a cooperative interplay between protein- and NA-mediated interactions that typify natural nucleoprotein assemblies. We report here a structurally well-defined synthetic nucleoprotein assembly that forms through the synergy of three types of intermolecular interactions: Watson−Crick base pairing, NA−protein interactions, and protein−metal coordination. The fine thermodynamic balance between these interactions enables the formation of a crystalline architecture under highly specific conditions.

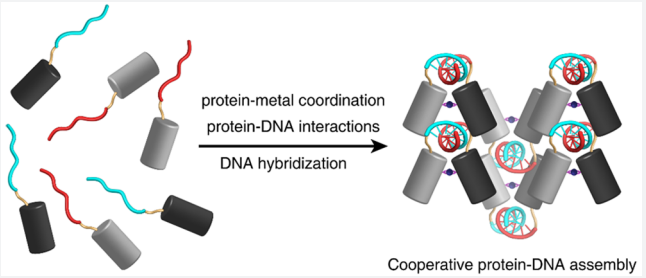

INTRODUCTION

Modularity is a key driver of biological complexity, whereby nature employs a limited set of building blocks to create strikingly diverse machines and materials. Hence, a prominent goal of synthetic biology and nanotechnology is to use biological or biomimetic building blocks (e.g., DNA or RNA, proteins, peptides, foldamers) in new structural contexts to construct self-assembled systems with properties that complement or surpass those produced by evolution. The emergence of the field of bio-nanotechnology has largely been fueled by the high fidelity of Watson−Crick base-pairing interactions, which have enabled the fabrication of DNA and RNA assemblies with complex structures that extend far beyond the natural scope of nucleic acids (NAs).[1−7] However, the inherent functional properties of these assemblies are restricted by the limited chemical scope of NAs. In parallel, there have been considerable efforts toward the design of artificial protein assemblies,[8−13] aiming to take advantage of the chemical and structural versatility of proteins. Synthetic protein assemblies have become sophisticated in terms of their architectures and functional attributes,[14−17] yet they still lack the facile structural programmability of NA-based assemblies. The complementary advantages and limitations of NA and protein building blocks prompt the obvious question: can proteins and NAs be combined modularly to form well-defined supramolecular assemblies?

Natural nucleoprotein assemblies such as ribosomes,[18] telomerases,[19] nucleosomes,[20] and gene-editing complexes[21] are inspiring examples in which protein and NA components are integrated into highly intricate yet monodisperse architectures. The disparate and nonuniform structures of these hybrid architectures highlight the complexity of the problem in hand: chemically and structurally, NAs and proteins are vastly dissimilar polymers, and there are no universal rules that dictate the interactions between them. In fact, synthetic approaches to create NA−protein hybrid architectures have generally relied on the immobilization of oligonucleotide-functionalized proteins or consensus NA-recognizing peptide sequences onto NA scaffolds[22−27] or the modification of proteins with long oligonucleotide chains to enable their self-assembly via base-pairing interactions.[28−30] While these strategies are effective for the spatial organization of protein units, the resulting architectures are mostly dominated by the NA components in terms of composition and mode of self-assembly, and unlike natural nucleoproteins, they possess little synergy involving protein−protein or

Received: October 12, 2018
Published: November 15, 2018

DOI: 10.1021/acscentsci.8b00745
ACS Cent. Sci. 2018, 4, 1578−1586

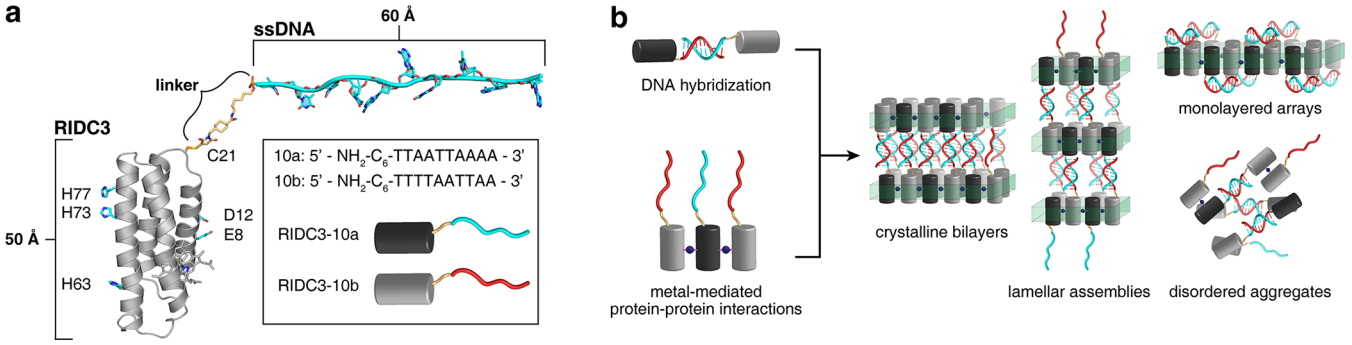

Figure 1. Design of RIDC3−10a/b. (a) Schematic of RIDC3−DNA hybrids. Metal-binding residues are shown as cyan sticks on the RIDC3 surface. (b) Potential self-assembly outcomes for the RIDC3−DNA hybrids.

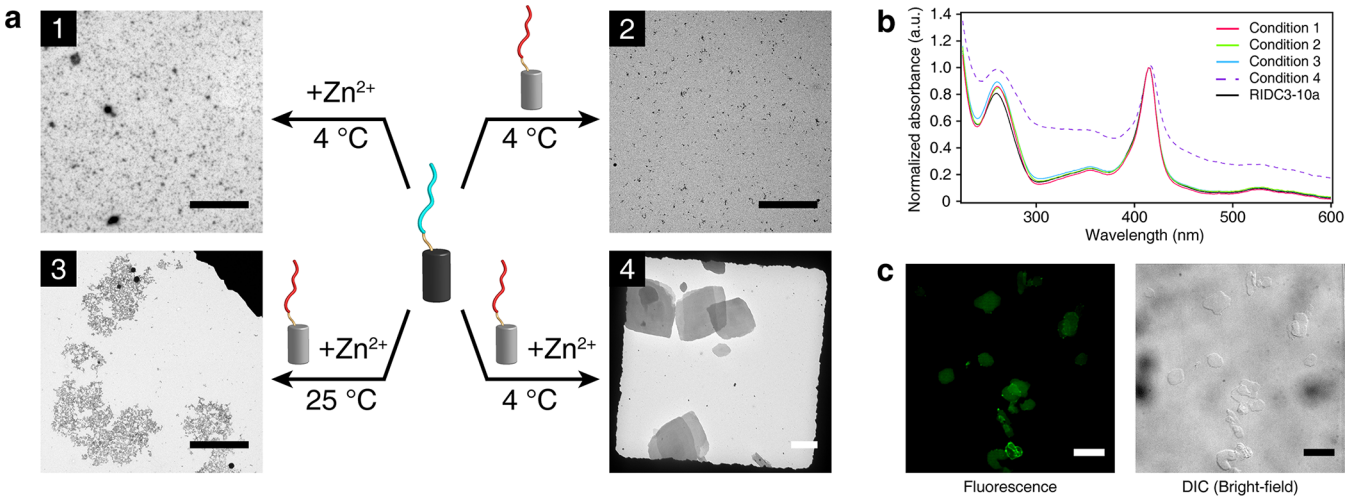

Figure 2. Initial characterization of self-assembled RIDC3−10a/b lattices. (a) TEM characterization of RIDC3−10a/b self-assembly under different conditions. (b) UV−Vis characterization of RIDC3−10a/b self-assembly under conditions shown in part a. Scattering of UV−Vis light is only observed for condition 4, indicating the formation of μm-scale structures. (c) Confocal microscopy images of RIDC3−10a/b crystals upon intercalation by SYBR Green. Scale bars in parts a and c are 5 and 10 μm, respectively.

protein−NA interactions. Recently, a hybrid system consisting of an engineered homodimer of a DNA-binding protein and cognate double-stranded DNA (dsDNA) sequences was reported,[31] but the resulting assemblies were limited to linear fibers devoid of substantial structural order.

RESULTS AND DISCUSSION

Design and Self-Assembly of DNA−Protein Chimeras.

In this study, we set out to create a synthetic nucleoprotein system whose self-assembly is governed by a cooperative interplay of protein- and DNA-mediated interactions. As the protein component, we chose RIDC3 (an engineered variant of the monomeric, four-helix bundle protein cytochrome cb_{562}, Figure 1a) which can self-assemble in a chemically tunable fashion into 1-, 2-, and 3D crystalline arrays through a combination of designed Zn^{2+}-mediated and non-covalent interactions.[12] RIDC3 was modified with a single cysteine residue at position 21 (C21) on a surface loop to enable covalent conjugation to single-stranded (ss) DNA sequences (Figure 1a).[32] We selected the DNA components to be (a) short, (<15 bases, melting temperatures (T_m) of 30 °C or below) such that they would approximately match the dimensions of the protein component and yield weak base-pairing interactions to promote self-assembly under thermodynamic control, and (b) non-self-associating, such that self-assembly is heterogenic, requiring two DNA−protein chimeras with complementary sequences.

^{C21}RIDC3 was quantitatively modified with complementary, nonslipping 10 bp DNA strands (10a and 10b; $T_{m,pred} \approx 7$ °C) to generate two hybrids, RIDC3−10a and RIDC3−10b (Figure S1). As depicted in Figure 1, RIDC3−10a and RIDC3−10b are essentially diblock copolymers (Figure 1a) with two domains whose self-assembly can be modulated by distinct stimuli and design parameters: DNA components primarily by oligonucleotide sequence and temperature, and protein components primarily by Zn^{2+} concentration and pH (to control the protonation of metal-coordinating residues). Given the proclivity of the RIDC3 components to form 2D layers,[12,33] we envisioned that there would be multiple potential outcomes for self-assembly based on the interplay of DNA- and protein-mediated interactions, including crystalline bilayers, lamellar assemblies, DNA-stapled monolayered arrays, and disordered aggregates (Figure 1b). To investigate the formation of ordered assemblies, we screened a variety of conditions (temperature, pH, absolute metal and protein concentrations, metal:protein molar ratios) using equimolar RIDC3−10a and RIDC3−10b (Figure S2). Ordered protein−DNA conjugate arrays (thin, μm-sized crystals) were observed only in a very narrow window of conditions: pH ranging from 4.75 to 5, temperatures of 4−10

DOI: 10.1021/acscentsci.8b00745
ACS Cent. Sci. 2018, 4, 1578−1586

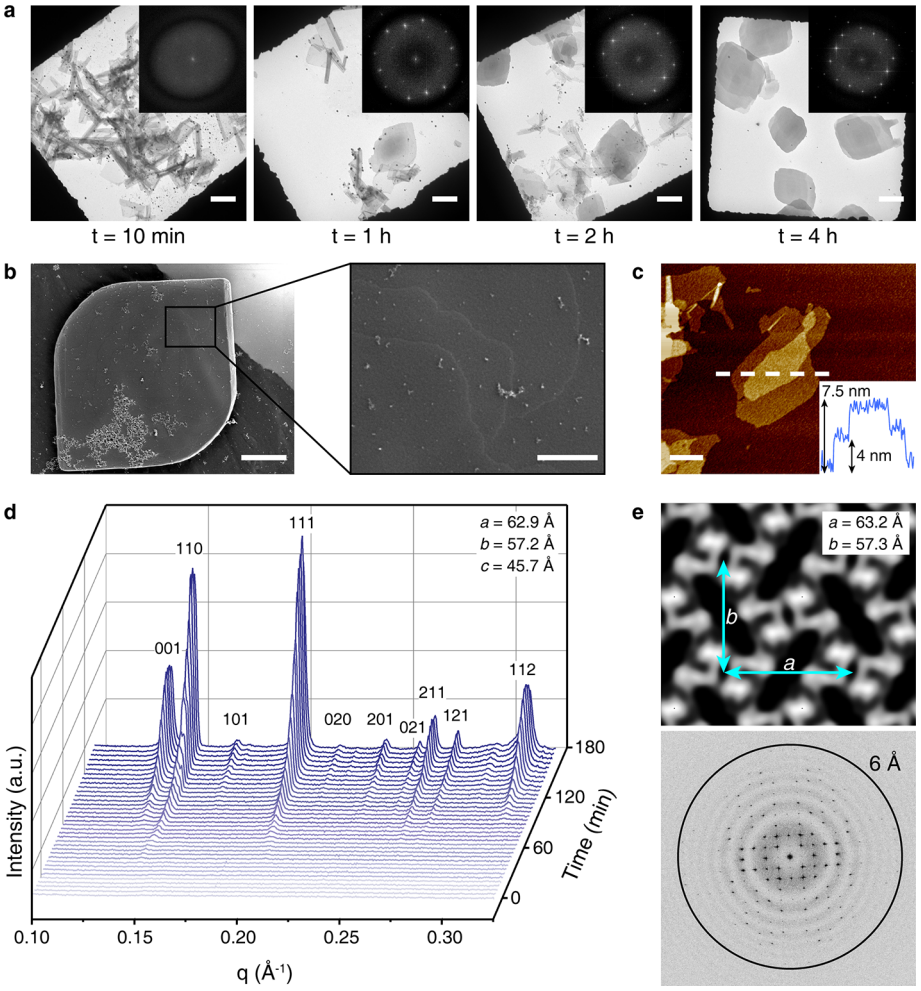

Figure 3. Characterization of the crystalline RIDC3−10a/b architecture. (a) Time-dependence of RIDC3−10a/b self-assembly as monitored by ns-TEM. Computed FFTs are shown as insets. (b) SEM micrograph of an RIDC3−10a/b crystal. Inset: magnification of boxed region to highlight the stacking of individual layers. Scale bars: 2 μm (image) and 500 nm (inset). (c) AFM image and height profile of two RIDC3−10a/b layers. Scale bar: 500 nm. (d) Time-dependent SAXS profiles of RIDC3−10a/b self-assembly. Miller indices are shown above the Bragg peaks. (e) Reconstructed 2D cryo-EM map (top) and computed FFT (bottom) of the RIDC3−10a/b architecture.

°C, and a molar ratio of [Zn^{2+}]:[total protein−DNA chimeras] between 2 and 10 (Figure 2a). Alternative conditions lying outside these windows typically gave rise to small (<100 nm in dimensions) clusters of disordered aggregates which did not scatter visible light (Figure 2b). Solutions lacking either chimera or Zn^{2+} did not yield any self-assembly products. Likewise, addition of the metal chelator ethylenediaminetetraacetic acid (EDTA) to suspensions of the RIDC3−10a/b crystals or their incubation at >40 °C immediately led to the dissolution of the crystals (Figure S3), implicating the involvement of both Zn^{2+}- and DNA-mediated interactions in self-assembly. A Job's analysis indicated that lattice formation was maximized at equal concentrations of RIDC3−10a and RIDC3−10b, as calculated by a quantitative analysis of protein incorporation into lattices (Figure S4). RIDC3−10a/b lattices became intensely fluorescent upon treatment with a cyanine dye that specifically binds dsDNA, providing strong evidence that dsDNA is an integral component of the architecture (Figure 2c, Figure S5).

Zn- and DNA-co-mediated self-assembly behavior of RIDC3−10a/b differs substantially from the Zn-mediated self-assembly of unmodified RIDC3, which yields crystalline arrays in a wide range of conditions, including pH values ranging from 5 to 8.5, temperatures ranging from 4 to 25 °C, and Zn:protein molar ratios between 2 and 100.[12] Whereas unmodified RIDC3 crystals took at least a day to emerge and a week to fully mature,[12] RIDC3−10a/b crystals formed quite rapidly with ordered assemblies appearing within 10 min and growing to μm dimensions within 4 h (Figure 3a). Negative-stain TEM (ns-TEM) measurements of RIDC3−10a/b lattices revealed a *pgg* plane group symmetry with unit cell parameters a = 60 Å, b = 59 Å, α = 90° in contrast to the *pg* symmetric RIDC3 crystals with a = 37 Å, b = 137 Å, α = 90° (Figure S6).[12] Taken together, these observations pointed to a fundamental alteration and increased chemical stringency in RIDC3 self-assembly through the inclusion of DNA interactions, and a new underlying molecular structure.

Structural Characterization of RIDC3−10a/b Lattices. Scanning electron microscopy (SEM) and atomic force microscopy (AFM) images of RIDC3−10a/b crystals showed that they consisted of ∼4 nm thick 2D layers that stacked up to a height of ca. 100 nm in 3D (Figure 3b,c; Figure S7). The small size and volume of the crystals led to weak X-ray diffraction, precluding 3D structure determination by crystallography. Nevertheless, small-angle X-ray scattering (SAXS) measurements on suspensions of RIDC3−10a/b crystals

DOI: 10.1021/acscentsci.8b00745
ACS Cent. Sci. 2018, 4, 1578−1586

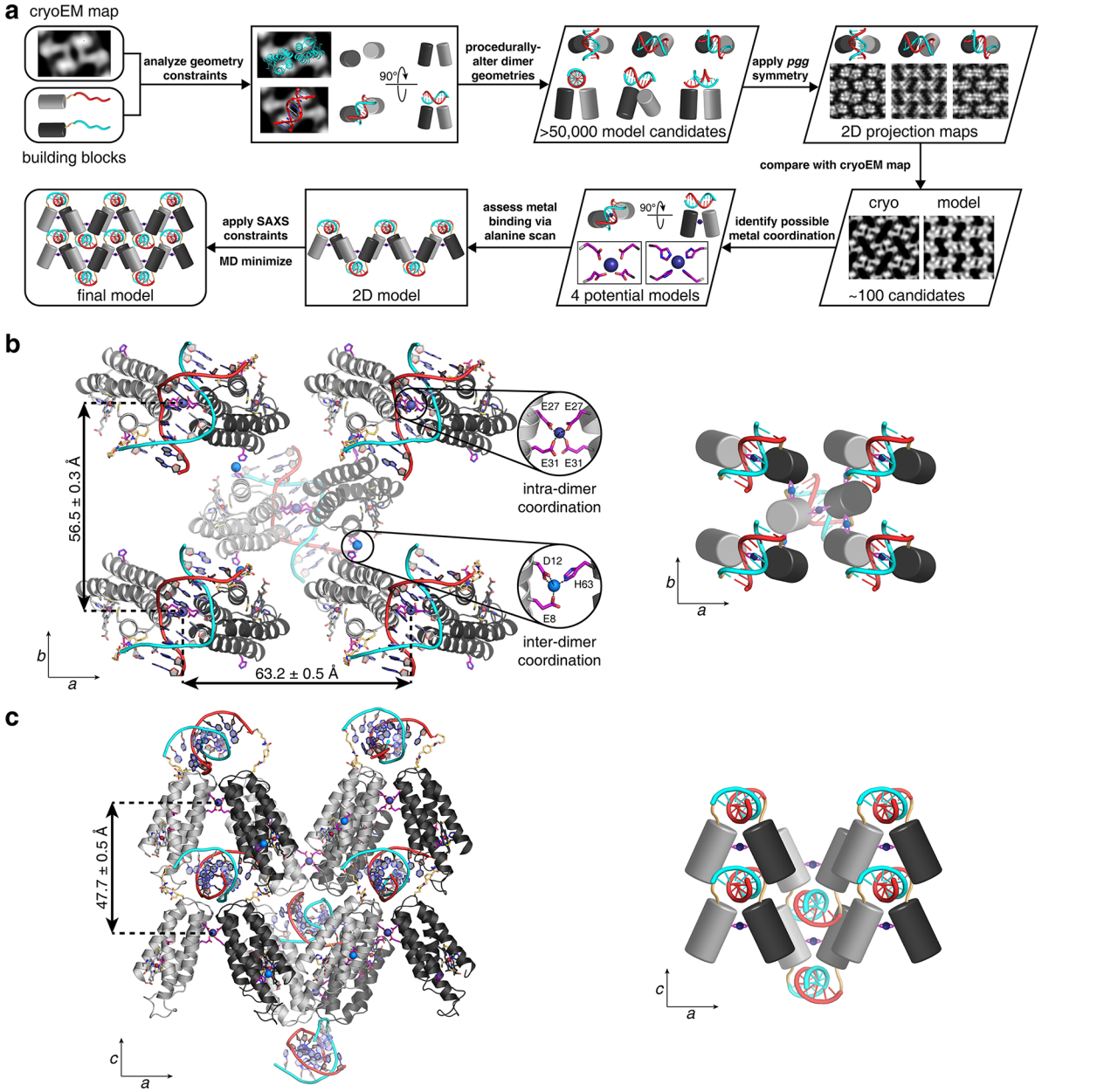

Figure 4. Structural modeling of the RIDC3−10a/b architecture. (a) Workflow detailing the generation of a 3D structural model of RIDC3−10a/b lattices. (b) MD-minimized model and cartoon illustration of a single 2D RIDC3−10a/b layer. (c) MD-minimized model and cartoon illustration showing the 3D stacking of two RIDC3−10a/b layers.

allowed us to determine the 3D symmetry and unit cell dimensions ($P2_12_12$; a = 62.9 Å, b = 57.2 Å, c = 45.7 Å) (Figure 3d). These parameters are notable in several regards. First, the a and b dimensions are in close agreement with those deduced from ns-TEM analysis, and the c dimension matches the step height (∼4 nm) observed in AFM experiments, confirming that RIDC3−10a/b crystals consist of discrete 2D molecular layers that stack up in 3D. Second, the $P2_12_12$ symmetry of the 3D unit cell is entirely consistent with the *pgg* symmetry obtained from 2D TEM analysis of the crystals, whereby the 2_1 screw axes along a- and b-dimensions (i.e., the xy-plane) translate into two perpendicular glide planes in a 2D projection. Importantly, the lack of a screw axis along the c-dimension (i.e., the z-direction) indicates that the 2D RIDC3−10a/b molecular layers are in perfect alignment and are not rotated with respect to one another along the c-axis. It thus follows that 2D TEM projection maps of RIDC3−10a/b crystals (aligned flatly on the grids) should correspond to the electron densities of individual 2D molecular layers.

Using first the ns-TEM images, we obtained 15 Å resolution projection maps that displayed an arrangement of continuous interconnected chains quite distinct from those of the Zn-mediated crystals of unmodified RIDC3 (Figure S6). Next, we turned to cryogenic electron microscopy (cryo-EM) measurements, which yielded ∼6 Å resolution images of RIDC3−10a/b lattices in a hydrated state (Figure 3e), with unit cell parameters (a = 63 Å, b = 57 Å, α = 90°) that closely approximate SAXS-determined values. Importantly, the cryo-EM projection maps were sufficiently detailed to allow us to build a plausible 3D structural model in combination with crystallographic constraints, the chemical knowledge of the

DOI: 10.1021/acscentsci.8b00745
ACS Cent. Sci. 2018, 4, 1578−1586

system in hand, and molecular dynamics (MD) simulations, as described below.

Construction of a 3D Structural Model for RIDC3−10a/b Lattices. To assess the molecular arrangement of proteins and DNA in the 2D crystals, we developed a workflow that enabled us to compare potential molecular orientations to the experimental 2D reconstruction map and generate model candidates (Figure 4a). We first focused on the basic repeat units of the lattice, which are dimers of L-shaped densities related to each other by the crystallographic 2-fold rotation axis normal to the 2D plane (i.e., the *z*-axis). Since the individual protein molecules do not have any internal symmetry, they cannot be placed on the symmetry axis, restricting each of the L-shaped halves to contain one or two protein units. Two-dimensional projected dimensions of the L-shaped densities (23 × 24 Å) can only accommodate a single four-helix bundle unit where the long axis of the protein is oriented approximately perpendicular to the 2D plane and therefore roughly parallel with the 2-fold symmetry axis; this establishes that each dimeric unit contains two protein molecules that are parallel—and not antiparallel—to one another (Figure S8). The glide reflections inherent in *pgg* symmetry further dictate that the neighboring dimeric units must be oriented in opposite directions to each other with respect to the *z*-axis, dictating an antiparallel arrangement of protein molecules across the interdimer interface.

Given this protein arrangement, the position of the DNA-anchoring Cys21 residues on each protein monomer, and the dimensions of the dimeric unit (37 Å across one diagonal and 55 Å across the other), we can conclude that (a) 10 bp dsDNA components (with approximate dimensions of 34 Å × 24 Å) must lie above and below the 2D lattice plane, and (b) their "projected" 2-fold rotational symmetry axis must coincide with the crystallographic 2-fold rotation axis, suggesting that the dsDNA strands must be oriented parallel to the 2D plane (Figure S8). With these constraints placed on each dimeric building block (which contains protein A, protein B, and an associated dsDNA), we generated >50 000 unique model structures, in which the protein A, protein B, and the dsDNA units were rotated and translated with respect to one another in *x*-, *y*-, and *z*-directions (Figure S9a,b). *Pgg* symmetry was further applied to generate a 2D lattice arrangement of the dimeric building blocks and to calculate a 2D projection map for each structural model (Figure S9c). These model electron densities were then examined to match features present in the experimentally measured maps. In particular, we noted that the projected map of a dsDNA unit lying parallel to the 2D crystal plane would give rise to a characteristic pattern with two parallel lines of electron density that overlays well with the long edges of the L-shapes within the dimer (Figure S10). Further, informed by previous experiments that established the necessity of Zn^{2+} coordination for protein−protein interactions,[10,12,34] we parsed the structural models for protein orientations that placed potential metal-binding residues in close proximity (side chain distances <5 Å).

This procedure yielded four candidates whose calculated projection maps captured the salient features of the experimentally determined map and which provided a set of plausible metal- and DNA-mediated protein−protein interactions to produce a continuously connected 2D lattice (Figure S11). A set of metal coordination motifs consisting of the following residues were identified in the models (Figure S11): Glu8−Asp12−His63 (Models 1 and 2), Glu18−Glu92 (Model 1), Glu27−Glu31 (Model 2), Asp60−His63 (Model 3), and His73−His77 (Model 4). To identify which of these motifs were required for self-assembly, a series of point mutations were generated to change residues of interest to alanine (Ala), thereby abolishing metal binding (Figure S12). After two rounds of mutations, we established Model 2 as the only system that fulfills all chemical and crystallographic requirements, while also yielding a computed 2D projection map that most closely approximates the experimental map. This 2D arrangement fits the experimentally determined cryo-EM and SAXS lattice constraints in *a* and *b*, so *z*-directional stacking (as determined by SAXS measurements) was applied to complete the model. The final 3D model was subject to MD minimization and equilibration to assess the existence of specific protein−protein and/or protein−DNA interactions.

The RIDC3−10a/b architecture consists of dimeric modules of RIDC3−10a and RIDC3−10b, linked to one another through dsDNA and a four-coordinate Zn-binding motif comprising two Glu27−Glu31 pairs (Figure 4b; Supporting Information, Movie S1). Each of these dimeric, chevron-shaped modules are connected to four neighboring modules (in an antiparallel fashion) through a tridentate Zn coordination motif consisting of Glu8, Asp12, and His63 side chains. This generates a 2D plane of proteins interconnected by Zn coordination with dsDNA "staples" above and below the plane, giving rise to a corrugated 2D sheet (Figure 4c). The metal content of the RIDC3−10a/b lattice was determined by using the fluorescent indicator 4-(2-pyridylazo)resorcinol (PAR), a strong Zn chelator. The measured value of ∼1.25 tightly bound Zn ions per protein monomer closely approximates the ratio of 1.5 expected from the structure. The corrugated arrangement allows the stacking of 2D sheets in register along the *z*-direction to yield $P2_12_12$ symmetry and an interplanar spacing of ∼47 Å as determined by SAXS measurements. At this spacing, the dsDNA components of each sheet wedge into the open protein−protein interfaces of the neighboring sheets and form close non-covalent contacts with the protein surfaces (Figure 4c). Thus, a fully integrated, 3D structural network is created through the synergy of DNA-, protein-, and metal-mediated interactions.

This synergy is manifested in the temperature-dependent behavior of RIDC3−10a/b lattices. Although temperatures less than 10 °C were required to initiate self-assembly (in accord with the predicted $T_m \approx 7$ °C of the 10a/10b duplex), once the lattices were formed, they maintained their crystallinity until ∼35 °C, at which point they rapidly disintegrated in a highly cooperative transition typical of the melting behavior of dsDNA (Figure S13). Upon recooling of the solution and incubation at <10 °C, RIDC3−10a/b lattices reformed. However, if excess (>8 molar equiv) single-stranded 10a or 10b was added as a competitor to the self-assembly mixture during recooling, no lattices were observed, confirming the involvement of DNA hybridization in RIDC3−10a/b lattice formation (Figure S14).

Computational Analysis of Protein−DNA Interactions within the RIDC3−10a/b Architecture. The preponderance of acidic residues participating in Zn^{2+} coordination is consistent with the low pH (4.75) required for the self-assembly of RIDC3−10a/b and distinct from the Zn-mediated self-assembly of unmodified RIDC3, which invariably involved Zn coordination to surface His residues (H63, H73, H77; Figure 1a) at higher pHs.[12] In addition, an inspection of the

DOI: 10.1021/acscentsci.8b00745
ACS Cent. Sci. 2018, 4, 1578−1586

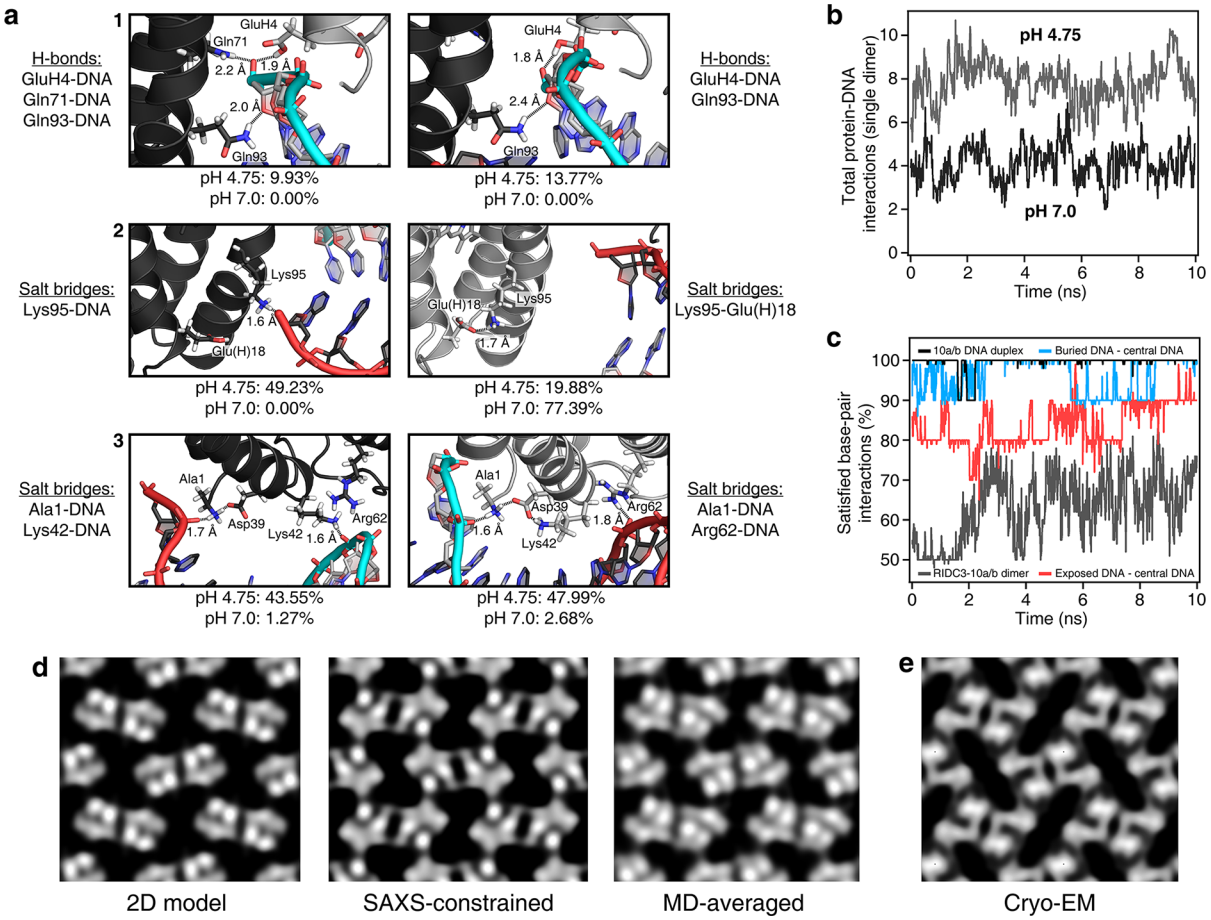

Figure 5. Molecular dynamics simulations of the RIDC3−10a/b lattice and comparison of calculated and experimental 2D projection maps. (a) pH-dependent protein−DNA interactions at pH 4.75 and 7.0 promoting 3D stacking. Percentages listed underneath each box indicate the relative occupancy (per RIDC3 monomer) of the depicted interactions during 10 ns of sampling at equilibrium for both pH 4.75 and pH 7.0. (b) Total protein−DNA interactions for a single dimer in the crystal bilayer plotted over 10 ns of simulation. (c) Fraction of satisfied base-pair interactions over time for an isolated (black trace) or RIDC3-conjugated (colored traces) 10a/10b duplex. (d) Calculated projection maps for RIDC3−10a/b Model 2 before (left) and after (center) adjustment to account for SAXS constraints, and from equilibrium MD simulations (right). (e) Experimental cryo-EM density map for the RIDC3−10a/b lattice.

protein surfaces that form interplanar contacts with the negatively charged dsDNA units indicates that they are also predominantly negatively charged at neutral pH (Figure S15). Therefore, the 3D stacking of RIDC3−10a/b layers can only be stabilized at acidic pH upon mitigation of the protein negative charge and activation of specific protein−DNA interactions, as corroborated by MD calculations (Figure 5). Simulations of a minimal bilayer crystal containing 10 dimeric units (i.e., two stacked sheets, each containing 5 dimers) revealed an intricate network of interactions arising from the protonation of surface-exposed Glu residues at pH 4.75, increasing contact with the DNA backbone both directly through H-bonding and indirectly by the release of basic residues from intraprotein salt bridges (Figure 5a). Interactions **1** and **2**, as shown in Figure 5a, highlight some direct consequences of side chain protonation at low pH, resulting in a severe reduction in interaction strength at pH 7.0 by favoring intraprotein salt bridging (Lys95−Glu18) and charge repulsion (Glu4−DNA), respectively. Common to both pH values is interaction network **3**, in which the protonated N-terminus of the protein associates with the DNA backbone, and Lys42/Arg62 provide redundant contacts to ensure a basal level of interaction; pH 7.0 most frequently exhibits singular Arg62−DNA interactions in place of the multivalent network observed at pH 4.75. This pattern is reflected in a nearly 2-fold increase in the number of total protein−DNA contacts at low pH (Figure 5b). MD simulations further showed that dimeric RIDC3−10a/b units could only maintain their structural integrity when placed in the context of the lattice and were not stable in isolation, as made evident by a ca. 20% increase in DNA base-pairing relative to a free dimer (Figure 5c, Figure S16). Notably, a superior approximation to the experimental cryo-EM map, relative to static models, was obtained from an averaged calculated 2D projection from the production trajectory (Figure 5d).

Effect of DNA Length and Sequence on RIDC3−DNA Self-Assembly. When equimolar RIDC3−10a and RIDC3−10b were incubated at 4 °C and pH 4.75, we only observed monomeric species in solution and no evidence of a stable dimer (Figure S17), showing that 10 bp DNA hybridization alone is not sufficiently strong to maintain a stable protein dimer. These findings again illustrate that the formation of the 3D structural network of RIDC3−10a/b lattices requires the cooperativity of three different types of interactions (metal-mediated protein−protein, DNA hybridization, protein−DNA). While the orthogonality of these interactions affords

DOI: 10.1021/acscentsci.8b00745
ACS Cent. Sci. 2018, 4, 1578−1586

a

DNA sequence pairs	Predicted T_m (°C)	2D crystal formation	ns-TEM lattice parameters
8a: TTGGTTAA 8b: TTAACCAA	6.3	none observed	N/A
10a: TTAATTAAAA 10b: TTTTAATTAA	7.1	pH 4.75 at 4 °C	a = 60 ± 1 Å, b = 58 ± 1 Å α = 90 ± 1°
10c: TATATAAAAT 10d: ATTTTATATA	3.9	pH 4.75 at 4 °C	a = 59 ± 1 Å, b = 56 ± 1 Å α = 93 ± 1°
12a: AAATCATCTAAG 12b: CTTAGATGATTT	24.5	pH 4.75 at 25 °C	a = 65 ± 1 Å, b = 55 ± 1 Å α = 90 ± 0.5°
15a: GCATCCTCTAAGATT 15b: AATCTTAGAGGATGC	40.4	none observed	N/A

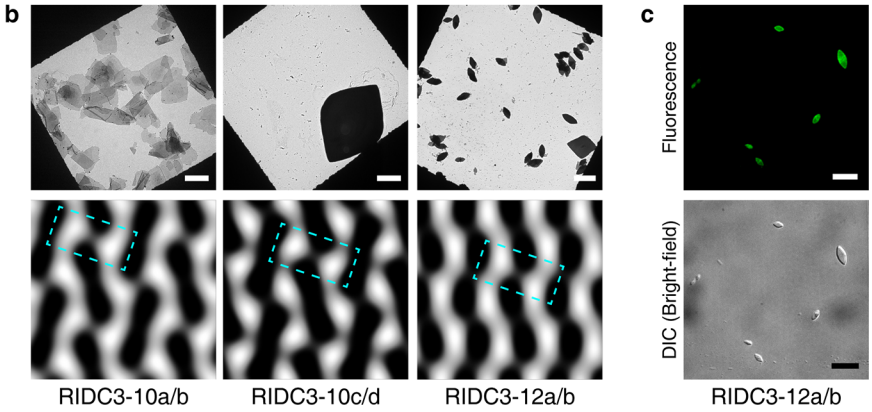

Figure 6. Characterization of various RIDC3−DNA constructs evaluated for self-assembly. (a) Tabulated parameters for all RIDC3−DNA conjugates. The predicted T_m of each duplex was calculated using OligoAnalyzer 3.1. (b) Representative ns-TEM micrograph and approximately 15 Å resolution 2D projection maps of RIDC3−10a/b, 10c/d, 12a/b. Similar features in projection maps are boxed in cyan. (c) SYBR-Green-incubated RIDC3−12a/b crystals brightly fluoresce, as seen in a fluorescence channel image and DIC (bright-field) image, indicating the presence of dsDNA. Scale bars for parts b and c are 5 and 10 μm, respectively.

self-assembly with high chemical specificity (i.e., in a very narrow window of conditions), their individual weakness allows for the reversibility and structural fluidity that is needed for the observed rapid assembly kinetics.

Finally, we investigated whether the hybrid lattices can accommodate variations in the DNA components to modulate self-assembly. To this end, we prepared four additional pairs of complementary RIDC3−DNA chimeras: one pair (RIDC3−10c and RIDC3−10d) which differs from the 10a and 10b chimeras in the order of DNA sequences, and three pairs (8a−8b, 12a−12b, and 15a−15b) which differ in both sequence and length (Figure 6a). As anticipated, RIDC3−10c and RIDC3−10d formed Zn-mediated crystalline arrays when paired with one another, but not when paired with RIDC3−10a or RIDC3−10b (Figure S18). RIDC3−12a/RIDC3−12b also formed crystalline arrays under the same solution conditions, but now at temperatures up to 25 °C, consistent with the higher $T_{m,pred}$ (~25 °C) of the 12a/12b duplex (Figure 6b,c). The experimentally determined lattice parameters of RIDC3−10c/d and RIDC3−12a/b crystals were slightly different than those of the RIDC3−10a/b crystals, but a comparison of the 2D electron density projection maps of the two lattices showed a nearly identical connectivity pattern (Figure 6b). This observation is consistent with the invariance of the Zn-mediated protein−protein interactions in the 2D plane and the ability of this lattice arrangement to accommodate a small elongation of the DNA staples afforded by the flexibility of the linkers between the protein and the DNA components (Figure S19). In contrast, we could not identify any experimental conditions under which the RIDC3−8a/8b ($T_{m,pred}$ < 6.3 °C) and RIDC3−15a/15b ($T_{m,pred}$ > 40 °C) pairs formed ordered assemblies. This is likely not only due to the steric incompatibility of very short (8 base pairs) or very long (15 base pairs) DNA staples with the lattice, but also due to significant alterations in the delicate energetic balance between DNA hybridization and Zn-mediated protein interactions necessary for crystalline self-assembly.

CONCLUSION

The functioning of a cell hinges upon the self-assembly of and communication between complex biopolymers in a crowded environment. The extremely high fidelity of these processes, in turn, necessitates a sophisticated chemical language that emerges from various combinations of biologically available non-covalent interactions. Along these lines, we have presented here a synthetic nucleoprotein assembly that combines three prominent classes of intermolecular interactions (Watson−Crick base pairing, DNA−protein interactions, protein−metal coordination) to self-assemble with high structural order and specificity in a manner that is reminiscent of natural nucleoproteins like the ribosome. While the modular nature of such multicomponent systems should offer distinct advantages in the construction of structurally tunable materials, the intricate architecture of the RIDC3−DNA assembly also highlights the opportunities and challenges inherent in designing artificial nucleoprotein complexes that arise from the distinct structural and chemical properties of proteins and NAs.

DOI: 10.1021/acscentsci.8b00745
ACS Cent. Sci. 2018, 4, 1578−1586

■ ASSOCIATED CONTENT

Supporting Information

The Supporting Information is available free of charge on the ACS Publications website at DOI: 10.1021/acscentsci.8b00745.

Additional experimental details and figures including FPLC chromatograms, ESI-MS spectra, TEM images, maximal monomer incorporation, absorbance measurements, fluorescent dye intercalation, SEM images, AFM images, structural models, SAXS profiles, electrostatic maps, sedimentation velocity profiles, and molecular weight distributions (PDF)

Movie S1: detailed views of the RIDC3−10a/b lattice from multiple angles, highlighting the metal-binding sites and 3D stacking (AVI)

■ AUTHOR INFORMATION

Corresponding Author

*E-mail: tezcan@ucsd.edu.

ORCID

Rohit H. Subramanian: 0000-0001-8750-7055

Sarah J. Smith: 0000-0001-6911-2383

F. Akif Tezcan: 0000-0002-4733-6500

Author Contributions

⊥R.H.S. and S.J.S. contributed equally to this work. S.J.S., R.H.S., and L.S. designed and performed most of the experiments and data analysis. R.G.A. and R.H.S. performed and analyzed MD simulations. G.C. and T.S.B. contributed to ns-TEM analysis. M.C. and H.S. contributed to cryo-EM data collection and analysis. J.B.B. and L.Z. performed SAXS experiments and data analysis. F.A.T. conceived and directed the project. F.A.T., R.H.S., S.J.S., and R.G.A. wrote the manuscript with comments from all authors.

Notes

The authors declare no competing financial interest.

Safety statement: no unexpected or unusually high safety hazards were encountered.

■ ACKNOWLEDGMENTS

We would like to thank the following colleagues for assistance: R. Anderson for assistance with SEM data collection; N. Gianneschi for use of AFM instrumentation; W.-J. Rappel for use of confocal microscope; K. Goldie, L. Kovacik, and R. Righetto for assistance with cryo-EM data collection and processing; T. Weiss and I. Rajkovic for assistance with SAXS measurements; D. Shi, J. De La Cruz, and T. Gonen for assistance with MicroED measurements; S. Joseph and A. Komor for helpful discussions. This work was primarily supported by the National Science Foundation (Division of Materials Research; DMR-1602537 to F.A.T.). Additional funding was provided by the U.S. Department of Energy (Division of Materials Sciences, Office of Basic Energy Sciences; DE-SC0003844 to F.A.T.; for MD simulations and partially for EM studies). R.H.S. was supported by the National Institute of Health Chemical Biology Interfaces Training Grant UC San Diego (T32GM112584-01). ns-TEM data were collected at the UCSD EM facilities supported by funding to T.S.B. from the NIH (R01-GM033050) and the Agouron Foundation. SAXS data were collected at Stanford Synchrotron Radiation Lightsource (SSRL), supported by the DOE Office of Science, Office of Basic Energy Sciences under Contract DE-AC02-76SF00515.

■ REFERENCES

(1) Seeman, N. C.; Sleiman, H. F. DNA nanotechnology. *Nat. Rev. Mater.* **2017**, *3*, 17068.

(2) Hong, F.; Zhang, F.; Liu, Y.; Yan, H. DNA Origami: Scaffolds for Creating Higher Order Structures. *Chem. Rev.* **2017**, *117* (20), 12584−12640.

(3) Rothemund, P. W. K. Folding DNA to create nanoscale shapes and patterns. *Nature* **2006**, *440*, 297−302.

(4) Ke, Y.; Ong, L. L.; Shih, W. M.; Yin, P. Three-Dimensional Structures Self-Assembled from DNA Bricks. *Science* **2012**, *338* (6111), 1177−1183.

(5) Wagenbauer, K. F.; Sigl, C.; Dietz, H. Gigadalton-scale shape-programmable DNA assemblies. *Nature* **2017**, *552*, 78−83.

(6) Geary, C.; Rothemund, P. W. K.; Andersen, E. S. A single-stranded architecture for cotranscriptional folding of RNA nanostructures. *Science* **2014**, *345* (6198), 799−804.

(7) Han, D.; Qi, X.; Myhrvold, C.; Wang, B.; Dai, M.; Jiang, S.; Bates, M.; Liu, Y.; An, B.; et al. Single-stranded DNA and RNA origami. *Science* **2017**, *358* (6369), No. eaao2648.

(8) Padilla, J. E.; Colovos, C.; Yeates, T. O. Nanohedra: Using symmetry to design self assembling protein cages, layers, crystals, and filaments. *Proc. Natl. Acad. Sci. U. S. A.* **2001**, *98* (5), 2217−2221.

(9) Ringler, P.; Schulz, G. E. Self-Assembly of Proteins into Designed Networks. *Science* **2003**, *302* (5642), 106−109.

(10) Salgado, E. N.; Radford, R. J.; Tezcan, F. A. Metal-Directed Protein Self-Assembly. *Acc. Chem. Res.* **2010**, *43* (5), 661−672.

(11) Sinclair, J. C.; Davies, K. M.; Vénien-Bryan, C.; Noble, M. E. M. Generation of protein lattices by fusing proteins with matching rotational symmetry. *Nat. Nanotechnol.* **2011**, *6*, 558−562.

(12) Brodin, J. D.; Ambroggio, X. I.; Tang, C.; Parent, K. N.; Baker, T. S.; Tezcan, F. A. Metal-directed, chemically tunable assembly of one-, two- and three-dimensional crystalline protein arrays. *Nat. Chem.* **2012**, *4*, 375−382.

(13) King, N. P.; Sheffler, W.; Sawaya, M. R.; Vollmar, B. S.; Sumida, J. P.; André, I.; Gonen, T.; Yeates, T. O.; Baker, D. Computational Design of Self-Assembling Protein Nanomaterials with Atomic Level Accuracy. *Science* **2012**, *336* (6085), 1171−1174.

(14) Song, W. J.; Tezcan, F. A. A designed supramolecular protein assembly with in vivo enzymatic activity. *Science* **2014**, *346* (6216), 1525−1528.

(15) Suzuki, Y.; Cardone, G.; Restrepo, D.; Zavattieri, P. D.; Baker, T. S.; Tezcan, F. A. Self-assembly of coherently dynamic, auxetic, two-dimensional protein crystals. *Nature* **2016**, *533*, 369−373.

(16) Votteler, J.; Ogohara, C.; Yi, S.; Hsia, Y.; Nattermann, U.; Belnap, D. M.; King, N. P.; Sundquist, W. I. Designed proteins induce the formation of nanocage-containing extracellular vesicles. *Nature* **2016**, *540*, 292−295.

(17) Butterfield, G. L.; Lajoie, M. J.; Gustafson, H. H.; Sellers, D. L.; Nattermann, U.; Ellis, D.; Bale, J. B.; Ke, S.; Lenz, G. H.; et al. Evolution of a designed protein assembly encapsulating its own RNA genome. *Nature* **2017**, *552* (7685), 415−420.

(18) Cate, J. H.; Yusupov, M. M.; Yusupova, G. Z.; Earnest, T. N.; Noller, H. F. X-ray Crystal Structures of 70S Ribosome Functional Complexes. *Science* **1999**, *285* (5436), 2095−2104.

(19) Lin, J.; Ly, H.; Hussain, A.; Abraham, M.; Pearl, S.; Tzfati, Y.; Parslow, T. G.; Blackburn, E. H. A universal telomerase RNA core structure includes structured motifs required for binding the telomerase reverse transcriptase protein. *Proc. Natl. Acad. Sci. U. S. A.* **2004**, *101* (41), 14713−14718.

(20) Eitoku, M.; Sato, L.; Senda, T.; Horikoshi, M. Histone chaperones: 30 years from isolation to elucidation of the mechanisms of nucleosome assembly and disassembly. *Cell. Mol. Life Sci.* **2008**, *65* (3), 414−444.

(21) Jinek, M.; Chylinski, K.; Fonfara, I.; Hauer, M.; Doudna, J. A.; Charpentier, E. A Programmable Dual-RNA−Guided DNA Endonu-

DOI: 10.1021/acscentsci.8b00745
ACS Cent. Sci. 2018, 4, 1578−1586

clease in Adaptive Bacterial Immunity. *Science* **2012**, *337* (6096), 816−821.
(22) Niemeyer, C. M. Semisynthetic DNA−Protein Conjugates for Biosensing and Nanofabrication. *Angew. Chem., Int. Ed.* **2010**, *49* (7), 1200−1216.
(23) Fu, J.; Yang, Y. R.; Johnson-Buck, A.; Liu, M.; Liu, Y.; Walter, N. G.; Woodbury, N. W.; Yan, H. Multi-enzyme complexes on DNA scaffolds capable of substrate channelling with an artificial swinging arm. *Nat. Nanotechnol.* **2014**, *9*, 531−536.
(24) Malo, J.; Mitchell, J. C.; Vénien-Bryan, C.; Harris, J. R.; Wille, H.; Sherratt, D. J.; Turberfield, A. J. Engineering a 2D Protein−DNA Crystal. *Angew. Chem., Int. Ed.* **2005**, *44* (20), 3057−3061.
(25) Praetorius, F.; Dietz, H. Self-assembly of genetically encoded DNA−protein hybrid nanoscale shapes. *Science* **2017**, *355* (6331), No. eaam5488.
(26) Delebecque, C. J.; Lindner, A. B.; Silver, P. A.; Aldaye, F. A. Organization of Intracellular Reactions with Rationally Designed RNA Assemblies. *Science* **2011**, *333* (6041), 470−474.
(27) Song, J.; Li, Z.; Wang, P.; Meyer, T.; Mao, C.; Ke, Y. Reconfiguration of DNA molecular arrays driven by information relay. *Science* **2017**, *357*, No. eaan3377.
(28) Brodin, J. D.; Auyeung, E.; Mirkin, C. A. DNA-mediated engineering of multicomponent enzyme crystals. *Proc. Natl. Acad. Sci. U. S. A.* **2015**, *112* (15), 4564−4569.
(29) McMillan, J. R.; Brodin, J. D.; Millan, J. A.; Lee, B.; Olvera de la Cruz, M.; Mirkin, C. A. Modulating Nanoparticle Superlattice Structure Using Proteins with Tunable Bond Distributions. *J. Am. Chem. Soc.* **2017**, *139* (5), 1754−1757.
(30) Kashiwagi, D.; Sim, S.; Niwa, T.; Taguchi, H.; Aida, T. Protein Nanotube Selectively Cleavable with DNA: Supramolecular Polymerization of "DNA-Appended Molecular Chaperones. *J. Am. Chem. Soc.* **2018**, *140* (1), 26−29.
(31) Mou, Y.; Yu, J.-Y.; Wannier, T. M.; Guo, C.-L.; Mayo, S. L. Computational design of co-assembling protein−DNA nanowires. *Nature* **2015**, *525*, 230−233.
(32) Kukolka, F.; Niemeyer, C. M. Synthesis of fluorescent oligonucleotide−EYFP conjugate: Towards supramolecular construction of semisynthetic biomolecular antennae. *Org. Biomol. Chem.* **2004**, *2* (15), 2203−2206.
(33) Brodin, J. D.; Carr, J. R.; Sontz, P. A.; Tezcan, F. A. Exceptionally stable, redox-active supramolecular protein assemblies with emergent properties. *Proc. Natl. Acad. Sci. U. S. A.* **2014**, *111* (8), 2897−2902.
(34) Brodin, J. D.; Smith, S. J.; Carr, J. R.; Tezcan, F. A. Designed, Helical Protein Nanotubes with Variable Diameters from a Single Building Block. *J. Am. Chem. Soc.* **2015**, *137* (33), 10468−10471.

DOI: 10.1021/acscentsci.8b00745
ACS Cent. Sci. 2018, 4, 1578−1586